



Studies on the thermal properties and flammability of polyamide 6 nanocomposites surface-modified via layer-by-layer deposition of chitosan and montmorillonite

Tomasz M. Majka¹ · Marcin Cokot¹ · Krzysztof Pielichowski¹

Received: 28 December 2016 / Accepted: 22 November 2017 / Published online: 30 November 2017
© The Author(s) 2017. This article is an open access publication

Abstract

In this work, layer-by-layer assembly technique has been employed to deposit cationic chitosan (CH) and anionic montmorillonite (MMT- Na^+) polyelectrolyte coatings on polyamide 6 (PA6). Without an additional surface treatment, 5, 10 and 20 bilayers of CH/MMT- Na^+ were successfully adsorbed on PA6 matrix as confirmed by XRD, ATR-FTIR and SEM–EDX results. The thermal stability was evaluated using TGA and DSC methods, and it was found that neat PA6 demonstrated better performance (by *ca.* 5 °C) and bilayers caused slightly delayed melting of PA6 crystalline phase. Some interesting results proving imparted flame retardancy by applied assemblies were obtained by vertical (VFT) and horizontal (HFT) flammability tests and microcalorimetric analysis (MCC) methods. It was found that all of the coated PA6 specimens have accomplished V-0 notes in VFT and the intensity of melt dripping reduced. According to MCC results, PA6 covered with 20 bilayers showed the highest reduction—up to 10% relative to reference material—in PHRR.

Keywords Polymer nanocomposites · Polyamide 6 · Flame retardancy · Layer-by-layer deposition

Introduction

The origins of thin-film coating of solids by layer-by-layer (LbL) technique date back to 1960s, when Iler [1] did pioneering research, followed by Decher and Hong [2]. Since then, many practical applications of this surface treatment method have been described, such as in electrochromic materials [3–5], controlled drug delivery [6, 7], composites with barrier properties towards oxygen [8–12], antireflective [13] and waterproof coatings [14–16], and antibacterial materials [17–19]. In principle, LbL assemblies arise from alternative dipping of substrates in, most often, water-based solutions of polyelectrolytes, which makes this method eco-friendly. By adjusting the process parameters, i.e. the kind of polyelectrolytes used [20], molecular mass [21], pH [22, 23], the presence of opposite ions [20, 24], ionic strength [25] and temperature [22, 26],

one can fabricate coatings with desired properties, ready for scaling up and automatization [27–31].

Layer-by-layer self-assembly of polyelectrolytes to impart flame retardancy to cotton textiles has been applied by Li et al. [32, 33] who have studied different hybrid inorganic–organic and all-inorganic systems, which—when exposed to flame source—build up protective residue over the surface, limiting the access of oxygen and heat. Carosio's and Mannen's research groups applied nanoparticles of aluminosilicates and zirconium phosphate which, deposited on synthetic fibres, completely or almost utterly diminished dripping of polymer melt [34–38]. Regardless of the kind of substrate, most of the modifications minimized heat and gas products release during pyrolysis and combustion. Further research efforts in this field are focused on effective intumescent flame retardants composed of blowing agent, acid source and carbon source, which altogether can show synergistic effects.

This work reports on the thermal properties and flammability of polyamide 6 nanocomposites surface-modified via layer-by-layer deposition of chitosan and montmorillonite. It is noteworthy that LbL technique could

✉ Tomasz M. Majka
tomaszmajka@indy.chemia.pk.edu.pl

¹ Department of Chemistry and Technology of Polymers,
Cracow University of Technology, ul. Warszawska 24,
31-155 Kraków, Poland

be an ecologically friendly alternative for electrospinning and electrospaying methods.

Experimental

Materials

Tarnamid® T-27 polyamide 6 (PA6) in the form of pellets was received from Grupa Azoty S.A. (Tarnów, Poland). According to producer specification, it is medium viscosity type of polymer, designed for highly durable elements, including thin-walled elements, formed by injection moulding as well as processing modified pellets by compounding method. Cloisite® 15A (Southern Clay Products Inc., the USA) montmorillonite (MMT) organophilized with 125 meq/100 g quaternary ammonium salt chloride (composed of ~ 65% C18, ~ 30% C16, ~ 5% C14 mixture of aliphatic chains) was used to prepare PA6 nanocomposite (PA6/15A). To create a 0.5% (m/v) cationic solution, chitosan (CH) (Sigma-Aldrich, Iceland) ($M_w = 50\text{--}190$ kDa, deacetylation degree 75–85%) was dissolved into 18.2 MΩ deionized water (DI) (Hipernet, Poland). Sodium montmorillonite (MMT- Na^+) (Dellite® LVF, Laviosa Chimica Mineraria, Italy) was dispersed in DI with 0.5% (m/v) to obtain an anionic mixture. Both mixtures were magnetically stirred overnight, and after that, pH of chitosan dispersion was adjusted to 4.0 ± 0.5 by adding 1 M hydrochloric acid solution (Chempur, Poland) or 1 M sodium hydroxide solution (POCH, Poland). pH of MMT- Na^+ dispersion was not additionally stabilized (9.8 ± 0.1).

PA6 matrix processing

PA6 pellets vacuum-dried at 80 °C for 6 h and organophilized layered silicate 15A were mixed in mass proportion 97:3 by mechanical shaking of batch in plastic container for 15 min. Later on, the batch was dosed into twin-screw counter-rotating laboratory extruder Thermo Scientific Haake PolyLab PTW 16/25 to form a nanocomposite with 150 rpm rotation speed. As a dosing device, Brabender DDSR20 feeder compatible with extruder, working at 45 rpm, was used. The temperature from feed end to die end ranged from 245 to 260 °C. The obtained strip was cooled in a water bath (18 °C) of 1.5 m length and 27 dm³ capacity, whereupon pelletized in a ZAMAK device. To reduce the thermal history, the same procedure was applied to pristine polyamide 6 resin. After one more vacuum-drying, two types of materials (PA6 and PA6/15A) were compression-moulded in laboratory press ZAMAK P-200 to form 15 × 15 × 0.3 cm sheets. 50–55 g of pellets were filled into mould and pressed at 250 °C under 20 MPa for 2.5 min. The sheets were cooled for 20 min

and cut into 15 × 1.3 × 0.3 cm bar specimens for fire testing. Thermal analysis (TGA and DSC) investigations were done on non-further-processed pellets.

Layer-by-layer deposition

Before depositing LbL assemblies on pellets, both materials were washed with DI. Bar specimens had been additionally immersed into 10% acetone solution prior to DI washing, and then, either pellets or bars were vacuum-dried at 80 °C for 2 h. All of the specimens were alternatively dipped into the positively and negatively charged solutions: to enhance adhesion, first dips in CH and MMT- Na^+ were set to 5 min, but subsequent dips lasted for 1 min. In case of pellets, to avoid material losses, specially designed polypropylene sieves, closed from top by aluminium sieves, were used for dipping procedure. After each adsorption step, the materials were washed with DI for 1 min in order to desorb weakly adsorbed surface modification and dried for 30 min at 80 °C. Some part of excessive amount of water was taken away using tissue paper. The scheme of described procedure is shown in Fig. 1. Each cycle was repeated until 5, 10 and 20 bilayers (BLs) were built on each specimen type. (For instance, PA6/15A/10BL denotes PA6/MMT nanocomposite with 10 bilayers deposited.)

Coating characterization

Crystalline structure of chitosan, PA6, PA6/15A and samples after surface treatment was studied by means of X-ray diffraction (XRD) technique. The XRD diffractograms were obtained using a Bruker® D2 PHASER with LynxEye™ detector with copper anode $K\alpha$ as a radiation source ($\lambda = 1.54184$ Å). All scans were done independently in the range of $2\theta = 1^\circ\text{--}10^\circ$ (space 0.1 mm) and $10^\circ\text{--}30^\circ$ (space 1 mm). The only exception was chitosan sample, which was measured in the range of $2\theta = 1^\circ\text{--}60^\circ$ with space 1 mm. 2θ angle increment during analysis was 0.02°. The voltage and the current of X-ray tube were 30 kV and 10 mA, respectively. The degree of crystallinity presented in Table 2 was determined using Eq. (1):

$$\chi_c = \frac{\Delta H_m}{(1 - x_n)\Delta H_{m,100\%}} \times 100\%, \quad (1)$$

where x_n is nanofiller content (0 for PA6, 0.03 for PA6/15A), ΔH_m —heat of melting of polymer under investigation, determined by DSC (J g^{-1}), and $\Delta H_{m,100\%}$ —heat of melting of 100% crystalline polymer (230 J g^{-1}).

ATR-FTIR (attenuated total reflectance–Fourier transform infrared) spectra of materials have been recorded before flammability tests using a PerkinElmer Spectrum 65 FT-IR spectrometer in the range of 4000–600 cm^{-1} at

ambient temperature. The apparatus was equipped with diamond crystal, and 32 scans were collected with 4 cm^{-1} resolution and 1 cm^{-1} data collection interval.

Cross section morphology of bar specimens was imaged using a JEOL JSM-6010LA scanning electron microscope (SEM) (accelerated voltage 10 kV). Prior to analysis, the materials were cut with microtome and gold-sputtered onto cross section surface. Similar procedure was applied to the sample residues after combustion. Energy-dispersive X-ray (EDX) analyser (10 kV accelerated voltage, $500\times$ magnification) was used to investigate the elemental composition of specimens before combustion.

Thermal analysis

Thermogravimetric analysis (TGA) was carried out using a Netzsch TG 209 apparatus at a heating rate $20 \text{ }^\circ\text{C min}^{-1}$ under inert argon gas atmosphere (gas flow rate $20 \text{ cm}^3 \text{ min}^{-1}$). About 5 mg of the sample was put in an opened corundum ($\alpha\text{-Al}_2\text{O}_3$) crucible and heated from 30 to $600 \text{ }^\circ\text{C}$.

Differential scanning calorimetry (DSC) profiles were recorded using a Mettler Toledo DSC823^e instrument. Calibration was performed with indium and zinc standards.

For the DSC measurements, 5 mg of sample was put into an alumina crucible, closed by pressing, and then examined under argon gas atmosphere (gas flow rate $20 \text{ cm}^3 \text{ min}^{-1}$) by increasing temperature from -50 to $300 \text{ }^\circ\text{C}$, followed by cooling from 300 to $-50 \text{ }^\circ\text{C}$ at a heating/cooling rate of $20 \text{ }^\circ\text{C min}^{-1}$.

Flammability tests

Vertical (VFT) and horizontal (HFT) flammability tests were conducted according to IEC 60695-11-10:1999 (UL-94) standard. Total burning time and rate of burning (unless material showed self-extinguishing effect in specified test conditions) were measured, and digital photographs were taken to depict characteristics of burning together with residues. Limiting oxygen index (LOI) measurement was performed according to DIN EN ISO 4589-2 using Concept Fire Testing Oxygen Index Module apparatus that lets us adjust concentration of oxygen in gas stream with 0.1% by volume accuracy. Nitrogen/oxygen mixture rate flow was stabilized at 10 L min^{-1} .

Combustion properties were also tested using micro-scale combustion calorimetry (MCC) according to ASTM

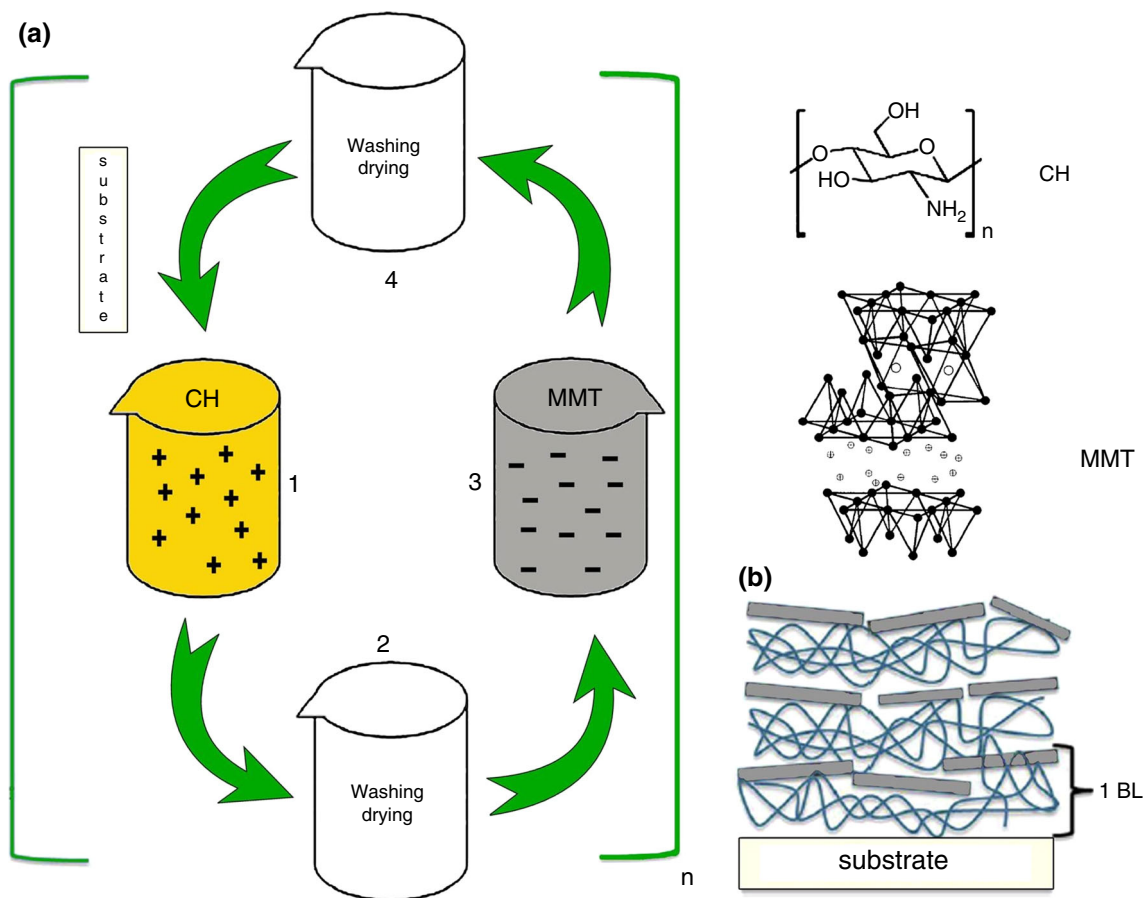


Fig. 1 **a** Procedure of layer-by-layer deposition; **b** components and cross section of ordered layers

D7309 standard with synthetic air. Mass of the samples was ca. 5 mg, and the heating rate was set at $1\text{ }^{\circ}\text{C min}^{-1}$.

Results and discussion

Coating growth and characterization

The XRD patterns of examined materials are shown in Fig. 2. Reflections visible in diffraction spectra in the range of $2\theta = 20^{\circ}$ – 24° are ascribed to crystalline phase of PA6 (Fig. 2c, e) [39]. As it is apparent from Fig. 2a, near 20° a peak resulting from the CH presence in LbL surface modification is expected. The observed shift of reflections at 21.3° for PA6 and at 21.6° for PA6/15A to lower angles right after deposition of coatings implies effective polycationic CH adsorption. Moreover, the peak at 23.4° (Fig. 2c), indicative of $\alpha 002/202$, is not well visible in Fig. 2e, but there is an appearance of a new shoulder near 24° instead. This shoulder shifts towards lower angles for BL materials and becomes slightly attenuated. Importantly, a similar shoulder can be seen at below $2\theta = 20^{\circ}$ only in diffraction patterns of BL samples. Overlapping of three patterns for BL modifications in Fig. 2e in the wide 2θ range led to the assumption of weak adsorption of MMT- Na^{+} to the PA6 substrate. Coating growth is hindered at just few nanolayers, which is observed as little or no intensity changes with consecutive dips, so in order to

achieve expected protective properties, it is not necessary to utilize long-lasting laboratory or industrial processes.

By analysing diffraction patterns of PA6/15A series (Fig. 2e), one can see peaks at 22° (PA6/15A) or at 21.5° (BL compositions) which can be deconvoluted to show $\gamma 001$, $\gamma 200$ and $\alpha 002/202$ crystalline forms. Such a characteristic pattern is not visible in Fig. 2c, suggesting that silicate incorporation into polymer matrix facilitates crystallization of PA6 in less thermodynamically stable, pseudo-hexagonal γ -form [40]. Because of space confinement, intermolecular hydrogen bonds are impeded to form as conformation of backbone chains alters from monoclinic α into γ . Coexistence of both forms can be also verified by analysis of the reflection in the range 10° – 11° , shifting to lower 2θ angles for BL materials due to overlaying with broad CH signal (Fig. 2a), which correspond to $\gamma 020$ plane.

It is worth paying attention to baseline shape of all LbL-modified materials in the range of 1° – 3° , which indicates that the adsorbed clay exists in the form of randomly spread, disordered nanoplatelets. Pristine PA6 diffraction pattern exhibits different behaviours: at 1.1° baseline grows rapidly, then, up to 2.7° , is similar to the clay-containing composites, and, finally, up to 3.5° , the rising trend can be noticed again. Eventually, it seems important to explain similarities between baseline shape in the 4° – 6° region for PA6/10BL and PA6/15A composites. Apparently, this number of bilayers (10) may be a limiting number to physically adsorb MMT- Na^{+} on non-spherical PA6

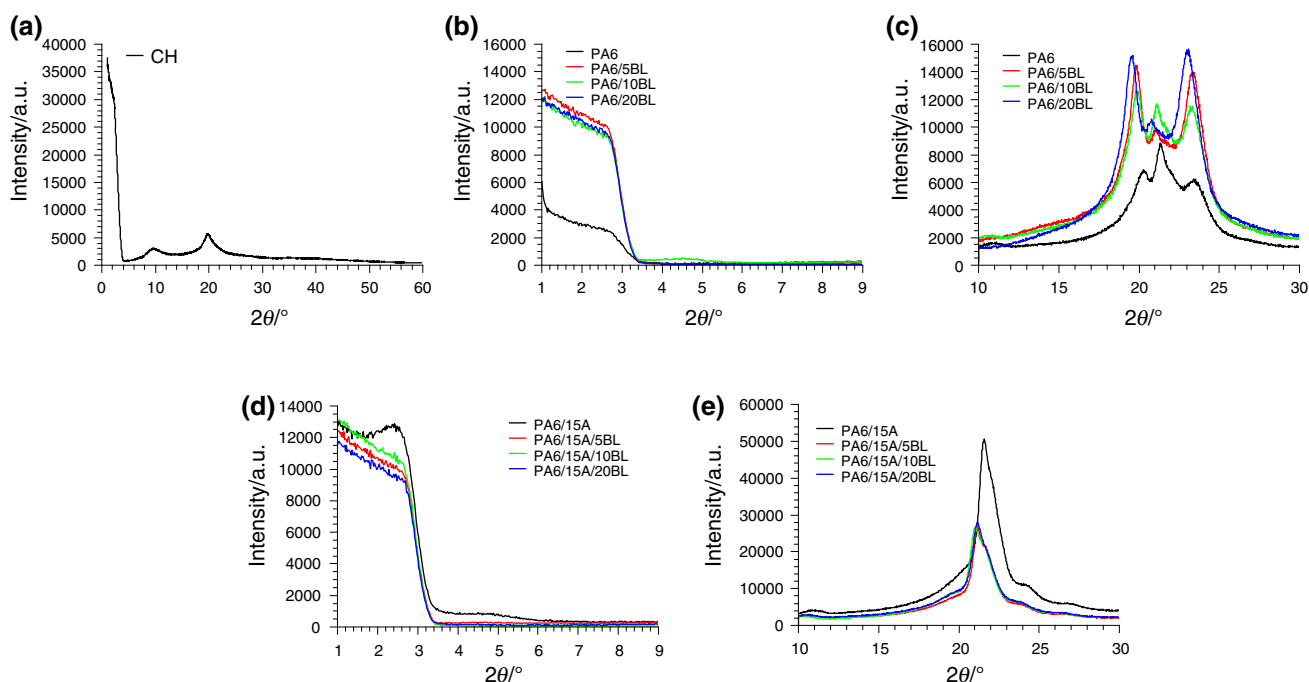
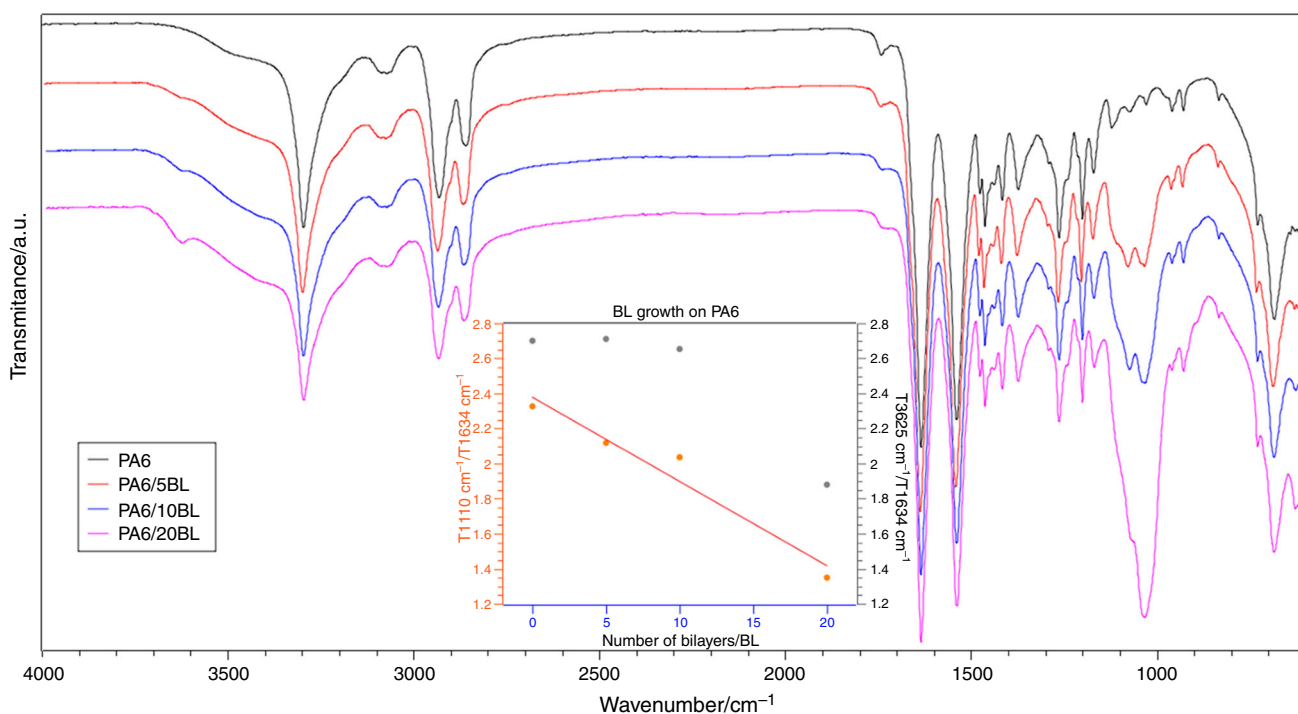
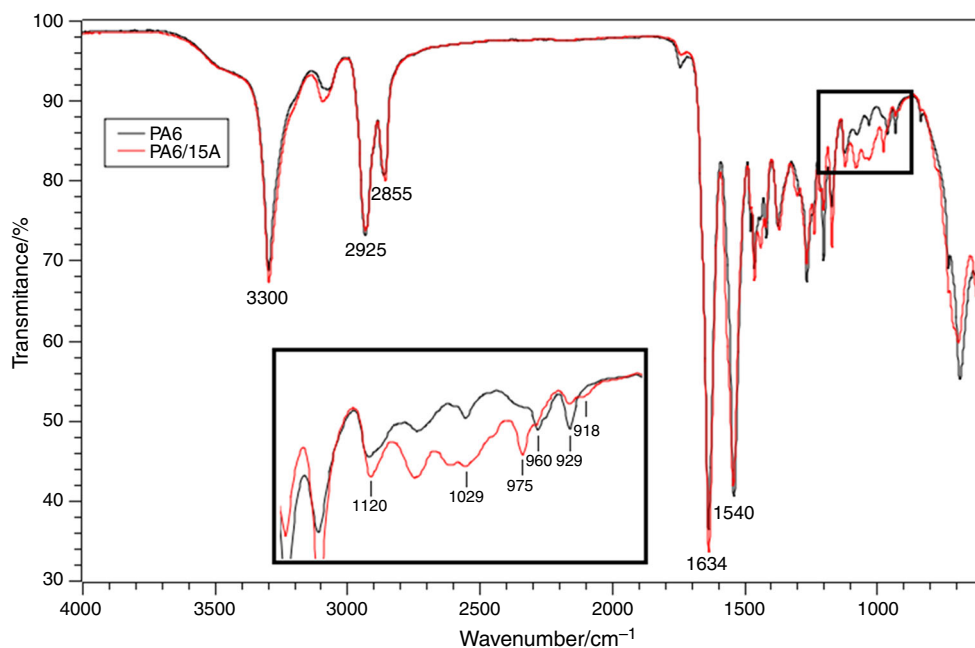


Fig. 2 XRD patterns of **a** chitosan (CH); **b** PA6 with 5, 10 and 20 bilayers in the range of 1° – 9° ; **c** PA6 with 5, 10 and 20 bilayers in the range of 10° – 30° ; **d** PA6/15A with 5, 10 and 20 bilayers in the range of 1° – 9° ; **e** PA6/15A with 5, 10 and 20 bilayers in the range of 10° – 30°

Fig. 3 Spectra of basal substrates (PA6 and PA6/15A)**Fig. 4** FTIR spectra of PA6 with 5, 10 and 20 bilayers and a diagram of transmittance ratio as a function of number of bilayers

substrate, observed as a series of reflections imitating those of layered silicates ($d \approx 2$ nm).

Supplementary data concerning incorporation of nanofiller into polyamide matrix were obtained from ATR-FTIR analysis of PA6 and PA6/15A materials (Fig. 3). In the IR spectra, band at 1540 cm^{-1} is assigned to deformation vibrations of N-H; band at 1634 cm^{-1} corresponds to

carbonyl moieties; and two peaks at $2800\text{--}2950\text{ cm}^{-1}$ are due to C-H stretching vibrations in alkyl groups. Nearby 3300 cm^{-1} , there is an absorption band of hydroxyl groups. Moreover, inter- and intramolecular hydrogen bonds are formed among PA6 chains between C=O and N-H groups of amide linkages.

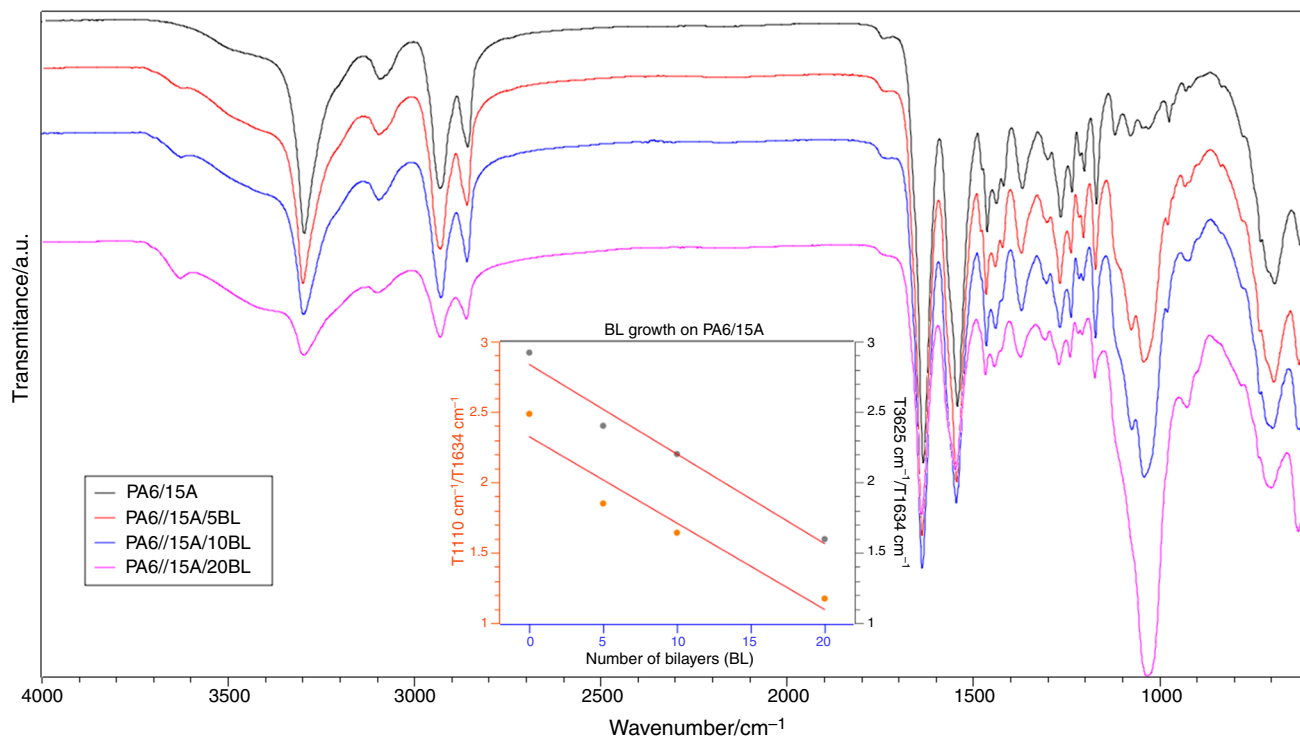
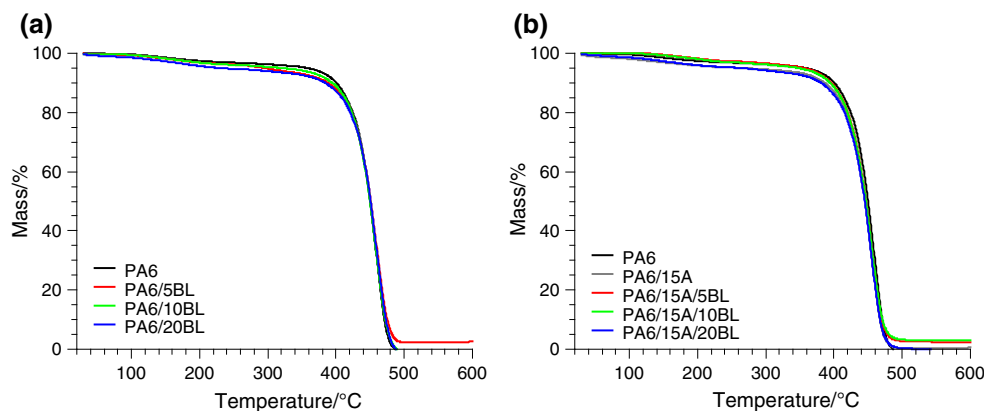


Fig. 5 FTIR spectra of PA6/15A with 5, 10 and 20 bilayers and a diagram of transmittance ratio as a function of number of bilayers

Fig. 6 TG profiles of PA6 (a) and PA6/15A (b) with 5, 10 and 20 bilayers



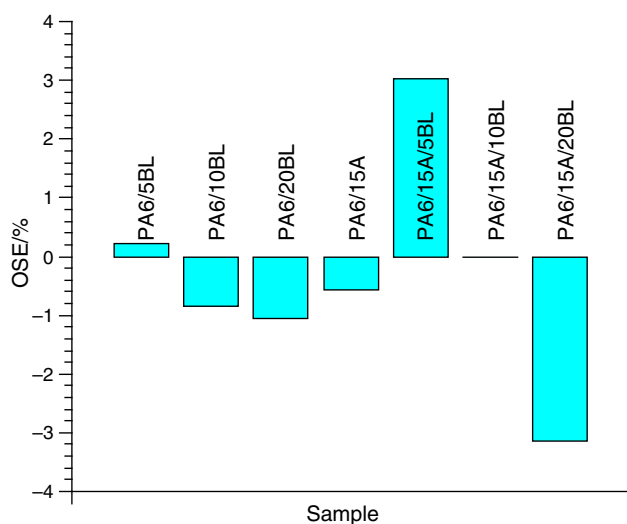
Formation of nanocomposite (PA6/15A) is confirmed by shape of signals at $1000\text{--}1150\text{ cm}^{-1}$. In montmorillonite spectrum, a broad band of Si–O bond stretching is visible in this region. Besides, a weak signal at 918 cm^{-1} originates from AlOH scission deformation. Figures 4 and 5 present FTIR spectra of all tested materials, in which some regular shifts are noticeable. With more bilayers deposited, the intensities of bands at $3200\text{--}3400\text{ cm}^{-1}$ (hydrogen bonds and OH groups) and at $2800\text{--}2950\text{ cm}^{-1}$ are increasing. A distinct change can be observed at $950\text{--}1150\text{ cm}^{-1}$, which corresponds to incorporation of polyelectrolytes onto polymeric substrates. As signals of virgin chitosan overlay with those of PA6 (symmetric and

asymmetric stretching of NH_4^+ at 1540 and 1635 cm^{-1} , respectively; planar deformations of N–H and C–N stretching at 1540 cm^{-1} ; scissoring vibrations of NH_4^+ at 1170 cm^{-1}), LbL modification effects require a detailed study of the latter region. Actually, band at 1110 cm^{-1} correlated with C–O–C stretching of glycoside linkage shows growth of intensity. (In the proximity in MMT spectrum, a broad Si–OH stretching signal is also visible.) Moreover, deposition of MMT- Na^+ can be evidenced by the appearance of band at 3625 cm^{-1} (Al–OH and Si–OH stretching).

To further describe coating build-up by self-assembly mechanism of nanolayers, relative intensities of

Table 1 Temperatures at which 5, 10, 20, 50% mass loss occurs for PA6 and PA6/15A nanocomposites

Sample	$T_{\text{onset (5%)}}$	$T_{(10\%)}$	$T_{(50\%)}$	T_{max}	Residue at 480 °C/%
CH	266	285	395	301	44.2
PA6	358	400	450	458	1.8
PA6/5BL	295	387	451	459	6.0
PA6/10BL	321	395	450	458	3.1
PA6/20BL	229	384	451	459	3.0
PA6/15A	267	386	445	455	1.8
PA6/15A/5BL	356	395	447	455	4.4
PA6/15A/10BL	348	394	447	455	5.2
PA6/15A/20BL	264	381	445	455	2.0

**Fig. 7** Overall thermal stabilization effect of LbL deposition in PA6

characteristic bands for utilized polyelectrolytes were calculated. Diagrams of transmittance ratio as a function of number of bilayers, namely C–O–C/C=O: $T_{1110} \text{ cm}^{-1}$ /

$T_{1634} \text{ cm}^{-1}$ and (Al–OH + Si–OH)/C=O: $T_{3625} \text{ cm}^{-1}$ / $T_{1634} \text{ cm}^{-1}$, are shown in Figs. 4 and 5. For all nanolayers with exception of MMT- Na^+ on PA6 substrate (known in the literature as exponential regime or two linear regimes with 10 BLs as a limiting bilayer number), values of these show linear trend. The exponential regime is commonly explicated by initial island-like evolution, followed by diffusional growth consisting of diffusion of single polyelectrolyte in or out of the thin film. This difference between two basal materials is going to be explained later in relationship to flame-retardant properties of both.

Thermal analysis

The thermogravimetric curves for the PA6 and PA6/MMT nanocomposites with different values of BLs are presented in Fig. 6a, b, respectively. The analysed results (in an atmosphere of inert gas) in terms of temperatures at which 5 ($T_{5\%}$), 10 ($T_{10\%}$), 20 ($T_{20\%}$), 50% ($T_{50\%}$) and maximum (T_{max}) mass loss occurs are given in Table 1.

These results show that by combining OMMT, CH and MMT it is not possible to thermally stabilize PA6 during the initial stages of decomposition. The combination of MMT with CH stabilizer leads to a decrease in the thermal stability of polyamide nanocomposites for both series of materials.

For the composite PA6/10BL, $T_{5\%}$ was equal to 321 °C. In contrast, the LbL deposition caused a decrease in the beginning of the degradation by 37 °C in relation to polyamide 6. In the range of 400–475 °C, these PA6 samples with 5, 10 and 20 BLs have decreased stability (in terms of lower mass loss) compared to the neat polymer.

In the range of 400–500 °C, depolymerization process takes place with emission of large amounts of ϵ -caprolactam [41–44]. This is important not only in terms of thermal stability, but also from the point of recycling of clay/PA6 composites. In the narrow range of 440–460 °C, the PA6 thermogravimetric curve overlapped with the TG profiles

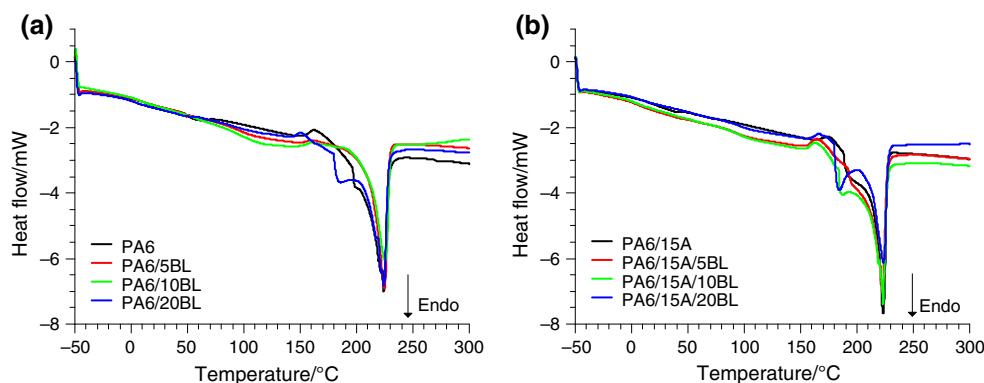
Fig. 8 DSC profiles of **a** PA6 and **b** PA6/15A with 5, 10 and 20 bilayers

Table 2 DSC parameters for PA6 and PA6/15A with 5, 10 and 20 bilayers

Sample	$T_m/^\circ\text{C}$	$T_c/^\circ\text{C}$	$\Delta H_m/\text{J g}^{-1}$	$\chi_c/\%$
PA6	220	185	62.28	26.0
PA6/5BL	222	182	63.22	
PA6/10BL	221	184	62.24	
PA6/20BL	221	184	62.09	
PA6/15A	220	185	66.09	28.4
PA6/15A/5BL	220	185	57.41	
PA6/15A/10BL	221	185	54.22	
PA6/15A/20BL	223	183	53.65	

Table 3 Limiting oxygen index results for PA6 and PA6/MMT with 5, 10 and 20 bilayers

Sample	LOI	ΔLOI
PA6	24.0	–
PA6/5BL	23.4	– 0.6
PA6/10BL	23.2	– 0.8
PA6/20BL	23.3	– 0.7
PA6/15A	23.2	–
PA6/15A/5BL	23.6	+ 0.4
PA6/15A/10BL	23.7	+ 0.5
PA6/15A/20BL	23.4	+ 0.2

of PA6/5BL, PA6/10BL and PA6/20BL. The main stage of degradation of these composites ended up near 470 °C, yielding some residues—Table 1. Thermogravimetric analysis (especially residue formation at 480 °C) has shown that the presence of bilayer inorganic–organic architectures strongly enhances the char formation. Furthermore, infrared spectroscopy has revealed that these coatings are able to promote the formation of a char having an aromatic nature. Depending on the number of layers, the organic–inorganic coatings are able to induce the formation of a thermally stable aromatic char that protects the polymer substrates from the application of a flame or different external heat fluxes.

Table 4 UL-94 data for PA6 and PA6/15A with 5, 10 and 20 bilayers (measurements taken in horizontal orientation)

Sample	Class	Burning time/s	Speed of burning/mm min ⁻¹	Amount of drips
PA6	Flammable	–	–	16
PA6/5BL	Non-flammable	–	–	5
PA6/10BL	Flammable	–	–	9
PA6/20BL	Flammable	–	–	8
PA6/15A	HB	208	21.6	19
PA6/15A/5BL	HB	295	15.3	18
PA6/15A/10BL	HB	276	16.3	23
PA6/15A/20BL	HB	252	17.9	18

Table 5 UL-94 data for PA6 and PA6/15A with 5, 10 and 20 bilayers (measurements taken in vertical orientation)

Sample	Class	Amount of drips
PA6	V-1	12
PA6/5BL	V-0	3
PA6/10BL	V-0	4
PA6/20BL	V-0	3
PA6/15A	–	11
PA6/15A/5BL	–	7
PA6/15A/10BL	–	7
PA6/15A/20BL	–	6

Thermograms presented in Fig. 6 show that within a temperature range of 350–460 °C, the PA6/15A nanocomposites had very similar mass loss and the similar thermal stability. The thermal degradation of polyamide composites (Fig. 6) takes place also in one step. T_{max} values of the composites containing the nanofillers and 5, 10 or 20 BLs are similar to and lower than those materials without 15A nanofiller.

At lower temperatures up to 120 °C, the observed mass loss is due to evaporation of physically adsorbed water, and water from hydrated ions is lost in the temperature range of 80–180 °C [45, 46]. The main stage between 200 and 470 °C is attributed to scission of HN-CO bonds, leading to the formation of unsaturated and saturated carbon–carbon bonds along the macrochain. Smaller amounts of residues in the range of 470–600 °C for all of systems reveal that there is less or no formation of ceramic-like structure by LbL deposition.

In order to afford a fair comparison of the effect of nanoparticles on polyamide, it is useful to define a thermal analysis parameter that is matrix independent. In this study, the overall stabilization effect (OSE) for PA6 and PA6/15A nanocomposites was calculated via integration of the area under the mass% versus temperature curves and is shown in Fig. 6a, b [47]:

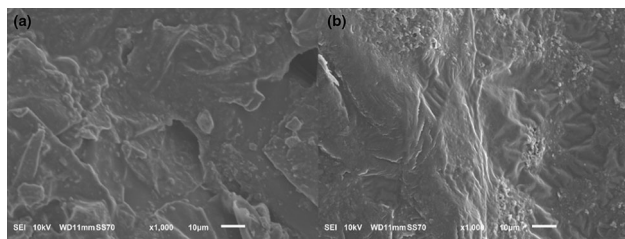


Fig. 9 SEM images of chars after the calorimetric test: **a** PA6/10BL; **b** PA6/15A/10BL

$$\text{OSE} = \sum_{T=20}^{605} ((\text{Mass percent of nanocomposite}_T) - (\text{Mass percent of neat polyamide}_T)) \quad (2)$$

where T is the degradation temperature.

A positive OSE value indicates an improvement in the overall thermal stability of the polymer nanocomposite in the temperature range 20–605 °C, while a negative value suggests that the overall thermal stability of the nanocomposite is inferior to that of the unmodified matrix. OSE values for PA6 and PA6/15A systems are presented in Fig. 7.

The OSE results reveal the combined stabilization action of clay or organoclay and CH stabilizer (5 BLs) on PA6. However, OSE values of all materials studied herein suggest that LbL technique itself is effective enough to yield PA6 materials with improved thermal stability.

The DSC curves for the PA6 and PA6/15A nanocomposites with different values of BLs are presented in Fig. 8a, b, respectively. The analysed results—melting temperature (T_m), crystallization temperature and degree of crystallinity—are given in Table 2.

The PA6/15A nanocomposite containing 3 wt% of organoclay has a higher ΔH_m as well as a higher proportion of PA6 crystalline phase. Under the processing conditions applied, the presence of the clay supports polymer crystallization. For nanocomposite materials, with the BL

increase, the melting enthalpy decreases. In general, the stack of nanolayers deposited on polymer substrate did not significantly influence the melting and crystallization temperatures, whereby the melting enthalpy for PA6/15A/BL materials is lower than for PA6/15A reference material. This effect may be explained by the protective action of BL influencing the melting behaviour of PA6 matrix.

Flame retardancy

LOI and UL-94 flammability tests are commonly used to study flame retardancy and burning characteristics of polymer materials. Values of both tests are listed in Tables 3–5. LOI results show that while surface-modified polyamide 6 materials require less of oxygen to steadily combust (compared to PA6), LOI of PA6/15A materials increases.

It has been observed that compositions based on PA6 burn with bright, natural flame and, up to self-extinguishment, polymer melt including charred products of degradation runs down slowly. Nanocomposite counterparts exhibit different behaviours, namely polymer melt distracts from the sample with flame and there is no self-extinguishment. Due to high viscosity of nanocomposite melt, it drops slower than in case of unfilled polymer, as well as irregularly, and the drops are bigger. Despite that, melt still burns and is capable of spreading fire. Improved flame retardancy of LbL modifications of PA6 were further confirmed by UL-94 tests.

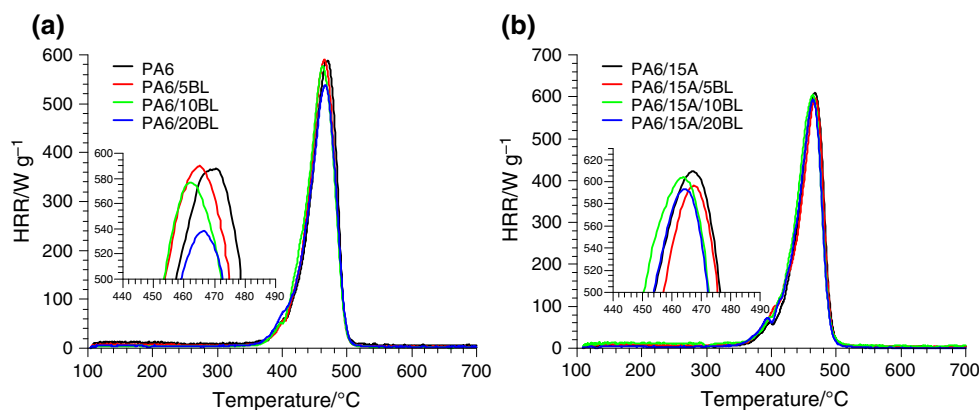
Although PA6 reference material self-extinguishes, the number of melt drops was at least twice higher than for LbL compositions. On the other hand, the latter burn slower, most effectively just with 5 BLs deposited (burning speed even 6 cm min⁻¹ slower than for PA6/15A). All PA6 BL modifications can pass V-0 rating at tested specimens, but pure PA6 shows V-1 only; in vertical test, both series present a decline in number of melt drops.

Charred residues of PA6/10BL and PA6/15A/10BL were analysed by SEM as shown in Fig. 9. Unfilled

Table 6 PHRR, temperature of PHRR, THR, percentage change of these in relation to references and FIGRA (the ratio of PHRR to temperature of PHRR) values for PA6 and PA6/15A with 5, 10 and 20 bilayers

Sample	PHRR/W g ⁻¹	$\Delta\text{PHRR}/\%$	THR/kJ g ⁻¹	$\Delta\text{THR}/\%$	FIGRA
PA6	587.7 (471 °C)	–	30.5	–	1.40
PA6/5BL	590.1 (465 °C)	+ 0.4	30.3	– 0.7	1.39
PA6/10BL	576.8 (462 °C)	– 1.9	30.7	+ 0.7	1.36
PA6/20BL	538.3 (466 °C)	– 8.4	29.1	– 4.6	1.30
PA6/15A	609.3 (467 °C)	–	30.3	–	1.46
PA6/15A/5BL	596.3 (468 °C)	– 2.1	29.9	– 1.3	1.42
PA6/15A/10BL	604.6 (464 °C)	– 0.8	31.6	+ 4.3	1.39
PA6/15A/20BL	593.4 (464 °C)	– 2.6	29.5	– 2.6	1.42

Fig. 10 HRR curves of **a** PA6 and **b** PA6/15A with 5, 10 and 20 bilayers



polymer modification has more irregular morphology of carbonaceous char than nanocomposite. It consists of loosely linked flakes and bubbles appearing during evolution of combustion gases and is comparable with original structure (Fig. 9b).

Microscale combustion calorimeter was used to explain the impact of surface modification on the intrinsic combustion properties by direct measurements of the heat released during controlled heating of samples. Table 6 lists the values of PHRR (maximum peak in heat release rate curve), temperature of PHRR, THR (total heat release), percentage change of these in relation to references and FIGRA (fire growth rate index—the ratio of PHRR to temperature of PHRR) as an important index of fire safety of polymer materials. The HRR curves are shown in Fig. 10. Of all studied samples, best parameters were found for PA6/20BL, which showed an improved thermal stability, as shown by TGA and DSC.

PA6/15A series start burning in lower temperatures (by about 20 °C) than PA6 (340 and 360 °C, respectively). Furthermore, the highest reduction in PHRR was demonstrated in materials with 20 BLs deposited, though none of them were higher than 10%. The temperatures of PHRR were not profoundly shifted with best results for 10BL modifications. With increasing number of bilayers, the parameter rises, which may reflect the existence of limiting thickness of coating, which shows minimum flame retardancy effect.

Conclusions

In this work, LbL assembly technique has been successfully employed to deposit cationic chitosan and anionic montmorillonite polyelectrolyte coatings on PA6 and its nanocomposite. It has been found that the coating growth is hindered at just few nanolayers, which is observed as little or no intensities change with consecutive dips, so in order

to achieve expected protective properties it is not necessary to utilize long-lasting laboratory or industrial processes. Deposition of MMT-Na + has been confirmed by IR spectroscopy through appearance of bands at 3625 cm^{-1} (Al–OH and Si–OH stretching) and at 918 cm^{-1} originating from AlOH scission deformations. The obtained TG profiles showed that within a temperature range of 350–460 °C, the PA6/15A nanocomposites had very similar mass loss and hence the similar thermal stability. The OSE results reveal the combined stabilization action of clay or organoclay and CH stabilizer (5 BLs) on PA6. The flammability results revealed that although the number of melt drops for PA6 reference material was at least twice higher than for LbL composites, the surface-modified PA6 materials burn considerably slower and can pass V-0 rating, whereas pristine PA6 shows V-1 behaviour only. MCC test results indicate that the temperatures of PHRR were maximally reduced for 10BL modifications, but with increasing number of bilayers, this parameter's value was increased. It may suggest that there is a critical thickness of coating, above which the flame retardancy effect is less profound.

Open Access This article is distributed under the terms of the Creative Commons Attribution 4.0 International License (<http://creativecommons.org/licenses/by/4.0/>), which permits unrestricted use, distribution, and reproduction in any medium, provided you give appropriate credit to the original author(s) and the source, provide a link to the Creative Commons license, and indicate if changes were made.

References

- Iler RK. Multilayers of colloidal particles. *J Colloid Interface Sci.* 1966;21:569–94.
- Decher G, Hong JD. Buildup of ultrathin multilayer films by a self-assembly process. *Makromolekular Symposia.* 1991;46:321–7.
- Liu S, Kurth DG, Möhwald H, Volkmer D. A thin-film electrochromic device based on a polyoxometalate cluster. *Adv Mater.* 2002;14:225–8.

4. Schmidt DJ, Pridgen EM, Hammond PT, Love JC. Layer-by-layer assembly of a pH-responsive and electrochromic thin film. *J Chem Educ*. 2010;87:208–11.
5. Sheng K, Bai H, Sun Y, Li C, Shi G. Layer-by-layer assembly of graphene/polyaniline multilayer films and their application for electrochromic devices. *Polymer*. 2011;52:5567–72.
6. Yan Y, Such GK, Johnston APR, Lomas H, Caruso C. Toward therapeutic delivery with layer-by-layer engineered particles. *ACS Nano*. 2011;5:4252–7.
7. Saurer E, Flessner R, Sullivan PS, Prausnitz RM, Lynn MD. Layer-by-layer assembly of DNA- and protein-containing films on microneedles for drug delivery to the skin. *Biomacromol*. 2010;11:3136–43.
8. Laachachi A, Ball V, Apaydin K, Toniazzo V, Ruch D. Diffusion of polyphosphates into (poly(allylamine)-montmorillonite) multilayer films: flame retardant-intumescent films with improved oxygen barrier. *Langmuir*. 2011;27:13879–87.
9. Yang YH, Haile M, Park YT, Malek F, Grunlan JC. Super gas barrier of all-polymer multilayer thin films. *Macromolecules*. 2011;44:1450–9.
10. Laufer G, Priolo MA, Kirkland C, Grunlan JC. High oxygen barrier, clay and chitosan-based multilayer thin films: an environmentally friendly foil replacement. *Green Mater*. 2013;1:4–10.
11. Tzeng P, Maupin CR, Grunlan JC. Influence of polymer interdiffusion and clay concentration on gas barrier of polyelectrolyte/clay nanobrick wall quadlayer assemblies. *J Membr Sci*. 2014;452:46–53.
12. Xiang F, Givens TM, Grunlan JC. Fast spray deposition of super gas barrier polyelectrolyte multilayer thin films. *Ind Eng Chem Res*. 2015;54:5254–60.
13. Shimomura H, Gemic Z, Cohen RE, Rubner MF. Layer-by-layer-assembled high-performance broadband antireflection coatings. *ACS Appl Mater Interfaces*. 2010;2:813–20.
14. Bravo J, Zhai L, Wu Z, Cohen RE, Rubner MF. Transparent superhydrophobic films based on silica nanoparticles. *Langmuir*. 2007;23:7293–8.
15. Xue C-H, Zhang L, Wei P, Jia S-T. Fabrication of superhydrophobic cotton textiles with flame retardancy. *Cellulose*. 2016;23:1471–80.
16. Wang S, Sui X, Xu H, Zhong Y, Zhang L, Mao Z. Flame retardant and water repellent finishing on cotton fabrics through a continuous layer by layer self-assembly technology. *Hans J Chem Eng Technol*. 2016;6:17–24.
17. Dvoracek CM, Sukhonosova G, Benedik MJ, Grunlan JC. Antimicrobial behavior of polyelectrolyte-surfactant thin film assemblies. *Langmuir*. 2009;25:10322–8.
18. Fang F, Chen X, Zhang X, Cheng C, Xiao D, Meng Y, Ding X, Zhang H, Tian X. Environmentally friendly assembly multilayer coating for flame retardant and antimicrobial cotton fabric. *Prog Org Coat*. 2016;90:258–66.
19. Fang F, Xiao D, Zhang X, Meng Y, Cheng C, Bao C, Ding X, Cao H, Tian X. Construction of intumescent flame retardant and antimicrobial coating on cotton fabric via layer-by-layer assembly technology. *Surf Coat Technol*. 2015;276:726–34.
20. Mermut O, Barrett CJ. Effects of charge density and counterions on the assembly of polyelectrolyte multilayers. *J Phys Chem B*. 2003;107:2525–30.
21. Sui ZJ, Salloum D, Schlenoff JB. Effect of molecular weight on the construction of polyelectrolyte multilayers: stripping versus sticking. *Langmuir*. 2003;19:2491–5.
22. Chang L, Kong X, Wang F, Wang L, Shen J. Layer-by-layer assembly of poly(N-acryloyl-N'-propylpiperazine) and poly(acrylic acid): effect of pH and temperature. *Thin Solid Films*. 2008;516:2125–9.
23. Shiratori SS, Rubner MF. pH-dependent thickness behavior of sequentially adsorbed layers of weak polyelectrolytes. *Macromolecules*. 2000;33:4213–9.
24. Zhang HN, Ruhe J. Interaction of strong polyelectrolytes with surface-attached polyelectrolyte brushes—polymer brushes as substrates for the layer-by-layer deposition of polyelectrolytes. *Macromolecules*. 2003;36:6593–8.
25. McAloney RA, Sinyor M, Dudnik V, Goh MC. Atomic force microscopy studies of salt effects on polyelectrolyte multilayer film morphology. *Langmuir*. 2001;17:6655–63.
26. Tan HL, McMurdo MJ, Pan GQ, Van Patten PG. Temperature dependence of polyelectrolyte multilayer assembly. *Langmuir*. 2003;19:9311–4.
27. Mateos AJ, Cain AA, Grunlan JC. Large-scale continuous immersion system for layer-by-layer deposition of flame retardant and conductive nanocoatings on fabric. *Ind Eng Chem Res*. 2014;53:6409–16.
28. Apaydin K, Laachachi A, Ball V, Jimenez M, Bourbigot S, Toniazzo V, Ruch D. Intumescent coating of (polyallylamine-polyphosphates) deposited on polyamide fabrics via layer-by-layer technique. *Polym Degrad Stab*. 2014;106:158–64.
29. Zhao L, Yan H, Fang Z, Wang J, Wang H. On the flameproof treatment of ramie fabrics using a spray-assisted layer-by-layer technique. *Polym Degrad Stab*. 2015;121:11–7.
30. Carosio F, Alongi J. Ultra-fast layer-by-layer approach for depositing flame retardant coatings on flexible pu foams within seconds. *ACS Appl Mater Interfaces*. 2016;8:6315–9.
31. Seo S, Lee S, Park YT. Note: automatic layer-by-layer spraying system for functional thin film coatings. *Rev Sci Instrum*. 2016;87:036110–3.
32. Li Y-C, Schulz J, Grunlan JC. Polyelectrolyte/nanosilicate thin-film assemblies: influence of pH on growth, mechanical behavior and flammability. *ACS Appl Mater Interfaces*. 2009;1:2338–47.
33. Li Y-C, Schulz J, Mannen S, Delhom C, Condon B, Chang S, Zammarano M, Grunlan JC. Flame retardant behavior of polyelectrolyte-clay thin film assemblies on cotton fabric. *ACS Nano*. 2010;4:3325–37.
34. Carosio F, Laufer G, Alongi J, Camino G, Grunlan JC. Layer by layer assembly of silica-based flame retardant thin film on PET fabric. *Polym Degrad Stab*. 2011;96:745–50.
35. Laufer G, Carosio F, Martinez R, Camino G, Grunlan JC. Growth and fire resistance of colloidal silica-polyelectrolyte thin film assemblies. *J Colloid Interface Sci*. 2011;356:69–77.
36. Carosio F, Alongi J, Malucelli G. α -zirconium phosphate-based nanoarchitectures on PET fabrics through layer-by-layer assembly: morphology, thermal stability and flame retardancy. *J Mater Chem*. 2011;21:10370–6.
37. Li Y-C, Mannen S, Schulz J, Grunlan JC. Growth and fire protection behavior of POSS-based multilayer thin films. *J Mater Chem*. 2011;21:3060–9.
38. Li Y-C, Mannen S, Morgan AB, Chang S, Yang Y-H, Condon B, Grunlan JC. Intumescent all-polymer multilayer nanocoating capable of extinguishing flame on fabric. *Adv Mater*. 2011;23:3926–31.
39. Dahiya JB, Rathi S, Bockhorn H, Haußmann M, Kandola BK. The combined effect of organic phosphinate/ammonium polyphosphate and pentaerythritol on thermal and fire properties of polyamide 6-clay nanocomposites. *Polym Degrad Stab*. 2012;97:1458–65.
40. Kiliaris P, Paspaspyrides CD, Xalter R, Pfaendner R. Study on the properties of polyamide 6 blended with melamine polyphosphate and layered silicates. *Polym Degrad Stab*. 2012;97:1215–22.
41. Bourbigot S, Samyn F, Turf T, Duquesne S. Nanomorphology and reaction to fire of polyurethane and polyamide nanocomposites containing flame retardants. *Polym Degrad Stab*. 2010;95:320–6.

42. Kashiwagi T, Du F, Douglas JF, Winey KI, Harris RH, Shields JR. Nanoparticle networks reduce the flammability of polymer nanocomposites. *Nat Mater*. 2005;4:928–33.
43. Visakh PM, Arao Y. Thermal degradation of polymer blends. *Composites and nanocomposites*. New York: Springer; 2015.
44. Alongi J, Carosio F, Malucelli G. Current emerging techniques to impart flame retardancy to fabrics: an overview. *Polym Degrad Stab*. 2014;106:138–49.
45. Monticelli O, Musina Z, Frache A, Belluci F, Camino G, Russo S. Influence of compatibilizer degradation on formation and properties of PA6/organoclay nanocomposites. *Polym Degrad Stab*. 2007;92:370–8.
46. Majka TM, Leszczyńska A, Pielichowski K. Thermal stability and degradation of polymer nanocomposites. In: Xingyi H, Chunyi Z, editors. *Polymer nanocomposites—electrical and thermal properties*. Hamburg: Springer; 2016. p. 167–90.
47. Katsoulis C, Kandare E, Kandola BK. The effect of nanoparticles on structural morphology, thermal and flammability properties of two epoxy resins with different functionalities. *Polym Degrad Stab*. 2011;96:529–40.